RSC Advances

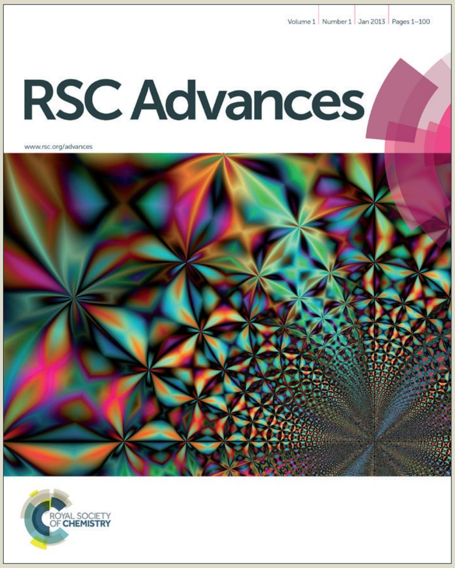

ROYAL SOCIETY OF CHEMISTRY

www.rsc.org/advances

Journal Name

ARTICLE

In-situ grown Nb_4N_5 nanocrystal on nitrogen-doped graphene as a novel anode for lithium ion battery †

Received 00th January 20xx,
Accepted 00th January 20xx

DOI: 10.1039/x0xx00000x

www.rsc.org/

Chenlong Dong[a], Xin Wang[a], Xiangye Liu[a], Xiaotao Yuan[a], Wujie Dong[a], Houlei Cui[b], Yuhang Duan[c], Fuqiang Huang[a, b,*]

Metal-rich niobium nitride of Nb_4N_5 has higher conductivity than Nb_3N_5 and higher theoretical specific capacity than NbN. To rationally design metal-rich anode material, Nb_4N_5 nanocrystal coated by nitrogen-doped graphene (N-G) has been successfully synthesized by a facile *in-situ* ice bathing method with subsequent annealing in NH_3. It is reported for the first time using as an anode material. The discharge capacity is 487 mA h g^{-1} at the current density of 0.1A g^{-1} (0.0819 mA cm^{-2})after 200 cycles and the high rate discharge capacity is 125 mA h g^{-1} at current density of 5A g^{-1} (4.0926 mA cm^{-2}). Specially, the discharge capacity still enhances after 200 cycles at 0.1A g^{-1} (0.0819 mA cm^{-2}). Nb_4N_5/N-G hybrid can be a promising anode material for LIBs with high rate performance and long cycle life.

Introduction

Lithium ion batteries (LIBs) have attracted considerable attention in the field of energy storage and conversion. The performance of LIBs is mainly determined by the properties of active electrode materials which are controlled by composition, structure, morphology and so on.[1] Commercial LIBs usually use graphite as anode. However, the theoretical capacity of graphite is severely limited to 372mA h g^{-1}, which limits its application for electrical/hybrid vehicles.[2-4] Generally, many metal oxides are explored as high capacity anode materials, however, they suffer from low conductivity. Compared to metal oxides, the metal nitrides often show improved conductivity. Therefore, the nitridation of metal oxides is a suitable method to acquire high performance anode materials.

Metal nitrides are emerging as promising electrode materials for high-performance LIBs[5, 6] due to their high Li^+ diffusion, excellent electrical conductivity[7] and flat potential close to that of lithium metal[8]. Niobium nitrides are mainly composed of Nb_3N_5, Nb_4N_3, NbN and some other nonstoichiometric niobium nitride compounds. Among them, the metal-rich phases (such as Nb_4N_5 and Nb_5N_6) have also been presented in δ-NbN system, which comprise lots of Nb^{5+} ions.[9, 10] They are promising candidates for LIBs because of their high-span valency transformation.[10]

Herein, we report the synthesis of Nb_4N_5/nitrogen-doped graphene hybrid nanomaterial (Nb_4N_5/N-G) by *in-situ* growth in ice bathing followed by NH_3 annealing. The as-prepared Nb_4N_5/N-doped graphene hybrid is reported for the first time using it as a LIBs anode material, which exhibits excellent electrochemical performance. Besides superior conductivity of Nb_4N_5, the internal defects between graphene layers motivated by the substitution of nitrogen atoms may enhance lithium storage.[11] Meanwhile, nitrogen-doped graphene can remit the expansion of Nb_4N_5 availably during discharge process and help forming stable solid electrolyte interface (SEI) layer. Therefore, the Nb_4N_5/nitrogen-doped graphene hybrid can be a novel promising anode for LIBs.

Experimental Section

Material

Niobium pentachloride was purchased from Aladdin Chemical Reagent. Anhydrous ethanol (> 99.7%) was purchased from Beijing Chemical Works. Ammonium hydroxide was purchased from Beijing Tong Guang Fine Chemicals Company. Graphene oxide was prepared according to the previous reported literature by Hummers[12] from graphite powder (purchased from Aldrich, powder, <20 micron). All used water in the process was deionized.

Material synthesis

Typically, 0.5489 g $NbCl_5$ was dissolved into 10 mL ethanol to form solution A. 90 g ice was added into 30 mL 3mg/mL GO solution (solution B) by vigorously magnetic stirring. The

---

[a] *State Key Laboratory of Rare Earth Materials Chemistry and Applications and Beijing National Laboratory for Molecular Sciences, College of Chemistry and Molecular Engineering, Peking University, Beijing 100871, P.R. China.*
[b] *CAS Key Laboratory of Materials for Energy Conversion, Shanghai Institute of Ceramics, Chinese Academy of Sciences, Shanghai 200050, P.R. China.*
[c] *Faculty of Science, Applied Chemistry Program, Beijing University of Chemical Technology, Beijing 100029, P.R. China.*

† Electronic Supplementary Information (ESI) available: Fabrication of graphene oxide (GO), TG-DSC analysis and calculation and coulombic efficiency of N-G at 0.1A g^{-1} (0.0832 mA cm^{-2}). See DOI: 10.1039/x0xx00000x

solution A was added into solution B dropwise. Then, the pH of mixed solution was adjusted to *ca.*7 by ammonium hydroxide. After centrifuging, the resulting Nb_2O_5/GO precipitate was washed by water for three times and freeze-dried for 12 h. Finally, the Nb_2O_5/GO was converted to Nb_4N_5/N-G by annealing in NH_3 at 700 °C under the flow rate of 350 mL/min for 4 h.

For comparison, the fabrication of Nb_4N_5 was similar to the above.

Physical Characterization

The microstructures were studied by scanning electron microscope (SEM) using a ZEISS Merlin Compact Field-emission scanning electron microscope (ZEISS, Germany) and transmission electron microscopy (TEM) used a JEM-2100 electron microscope (JEOL Ltd., Japan) working at 200 kV. The surface chemical composition was studied by X-ray Photoelectron Spectroscopy using Axis Ultra Imaging Photoelectron Spectrometer (Kratos Analytical Ltd., Japan). X-ray diffraction (XRD) was performed on a D8 Focus diffractometer with monochromatized Cu Kα radiation (λ =1.5418 Å). Raman spectrum was measured using a Renishawi instrument *via* Raman Microscope with laser excitation at 532 nm. Nitrogen adsorption isotherms were measured using a Micromeritics ASAP 2020 analyzer at 196 C. The weight of the sample used in the measurement was 100-200 mg. The Brunauer-Emmett-Teller (BET) method was utilized to calculate the specific surface area.

Electrochemical tests

To prepare the working electrodes, the Nb_4N_5/N-G, Nb_4N_5 and N-G were mixed with carbon black (Super P) and polyvinylidene fluoride binder with a ratio of 8:1:1 in N-methyl-2-pyrrolidone (NMP) to form slurry, respectively. The three slurries were coated onto copper foil. The coated foil was cut into disk electrodes of 14 mm in diameter. Then the electrodes were vacuum-dried overnight at 120 °C. Lithium foil (China Energy Lithium Co., Ltd.) was used as the counter and reference electrode. A glass fiber from Whatman was used as separator. The electrolyte was 1 $MLiPF_6$ in a 50:50 (w/w) mixture of ethylene carbonate (EC) and dimethyl carbonate (DMC). Coin Cell (LIR-2016 type) assembly was carried out in a recirculating an Argon glovebox where both the moisture and oxygen contents were below 1 *ppm*. All the cells were cycled between 0.01 and 3 V (*vs.* Li/Li^+) at certain current densities on a LAND CT2001A battery test system. The rate capability was evaluated by varying the current density from 0.1 A g^{-1} to 5 A g^{-1}. Specific capacities were calculated based on the mass of the each activated materials. Cyclic voltammetry (CV) was obtained on a CHI1000C electrochemistry workstation at the scan rate of 0.3 mV/s and the potential from 0.01 to 3 V (*vs.*Li^+/Li). The electrochemical impedance spectrum was obtained on the CHI600E with amplitude of 10 mV in the frequency range from 100 kHz to 0.01 Hz.

Results and discussion

Characterization

XRD patterns of Nb_4N_5, N-G and Nb_4N_5/N-G are shown in Figure1. The as-synthesized pure N-G displays a broad diffraction peak of (002) at 27.5° which is assigned to wrinkle layer-to-layer distance.[13] The diffraction peaks of pure Nb_4N_5 at 36.1°, 41.7°, 60.9°, 73.2°, 76.4° are indexed to (211), (310), (312), (213) and (422) crystal lattices, respectively (JCPDS No.51-1327, I4/m). The Nb_4N_5/N-G diffraction peak curve is higher than pure Nb_4N_5 from 25° to 35° because of the peak overlay of N-G and Nb_4N_5. Then, the Nb_4N_5/N-G hybrid is confirmed by Raman spectroscopy. As shown in Figure 2b, two broad peaks emerge at 1340 and 1590 cm^{-1} which are attributed to D and G bands of nitrogen-doped graphene, respectively. The D band strongly associates with the disorder degree of graphene.[14, 15] The G band corresponds to the zone center E_{2g} mode related to phonon vibrations in sp^2 carbon materials.[16, 17] Clearly, the I_D/I_G ratio (1.1:1) indicates the presence of a large amount of defects in the graphene layer due to the doping of nitrogen atoms. The Raman spectrum reveals that nitrogen-doped graphene with crystalline structures and many defects are obtained, which are favorable for the electrochemical properties.[18]

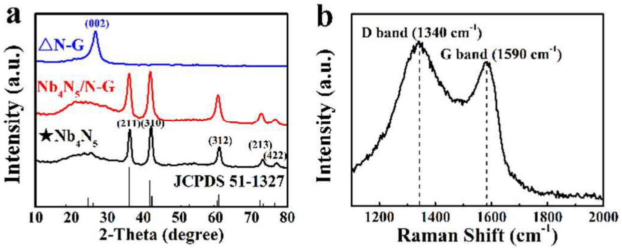

Figure 1. (a) XRD patterns of Nb_4N_5, N-G and Nb_4N_5/N-G hybrid; **(b)** Raman spectrum of Nb_4N_5/N-G hybrid.

The morphology of Nb_4N_5/N-G hybrid is characterized by SEM and TEM, as shown in Figure 2. The typical wrinkle structure of N-G is clearly observed in Figure 2a, which results from thermodynamically spontaneous bending. Meanwhile, the nanocrystals of Nb_4N_5 are tightly captured by the N-G. Figure 2b further confirms that the nanocrystals of Nb_4N_5 are uniformly dispersed on N-G without severe aggregation because of the protection of N-G. The SAED pattern (Figure 3c) can further confirm the high crystallinity of Nb_4N_5/N-G. These diffraction rings can be indexed to (312) of Nb_4N_5, (002) of N-G and (220) of Nb_4N_5 which are well in accordance with XRD patterns (Figure 1a).

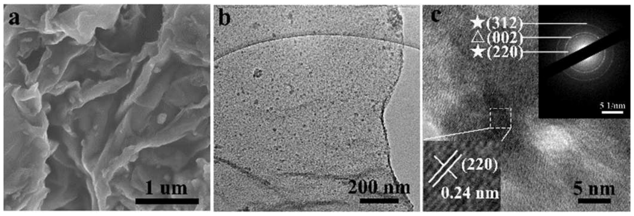

Figure 2. (a) SEM image of Nb_4N_5/N-G hybrid; **(b)** Low-magnification TEM image of Nb_4N_5/N-G hybrid; **(c)** High-magnification TEM image of Nb_4N_5/N-G hybrid. (NOTE: △and ★stand for N-G and Nb_4N_5, respectively).

X-ray photoelectron spectroscopy (XPS) measurement is performed to study the surface chemical composition and oxidation state. As shown in Figure 3a, the XPS survey spectrum shows that there are four elements: C, N, Nb and O without other impurity. Nb 3*d* spectrum involves two distinct doublets and a weak shoulder peak (Figure 3a). The highest Nb $3d_{5/2}$ binding energy at 207.0 eV can be indexed to the Nb^{5+}-O due to the oxidation of surface. The lowest binding energy emerges at 203.8 eV which belongs to the Nb $3d_{5/2}$ in Nb_4N_5 and the peak located at 205.0 eV can be indexed to Nb^{5+}-N.[19-21] The peaks at 206.3, 208.0 and 209.9 eV correspond to Nb $3d_{3/2}$. The C 1*s* spectrum is displayed in Figure 3b, which mainly exhibits three conspicuous peaks. The obvious core level peak binding energy at 284.9 eV represents graphite-like sp^2 C-sp^2 C, indicating that the most parts of carbon atoms exist in conjugated lattice.[18] The relatively weak peaks binding energy at 285.7 and 286.6 eV can be ascribed to N-sp^2 C and N-sp^3 C, respectively, because of N atoms and the defects.[22] The results of N-sp^2 C and N-sp^3 C correspond with the Raman analysis. As shown in Figure 3d, The broad N *1s* XPS peak can be fitted to the five peaks of Nb–N (396.9 eV), pyridinic N (398.5 eV), pyrrolic N (399.8 eV), graphitic N (401.5 eV) and oxygenated N (402.8 eV).

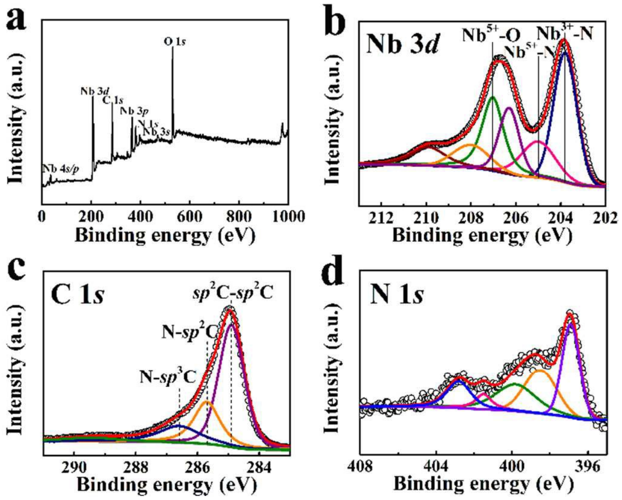

Figure 3. (a) XPS survey. High-resolution Nb_4N_5/N-G XPS spectrum of **(b)** Nb *3d*, **(c)** C *1s* and **(d)** N *1s* . The black scatter is the raw date and the red curve is the sum of different fitting peaks.

To investigate the content of N-G in Nb_4N_5/N-G, the TG-DSC measurement was carried out. As shown in Figure 4, the weight increase from *ca.* 150 to *ca.* 400 °C because the 1 molecular Nb_4N_5 is oxidated to be 2 molecular Nb_2O_5. After then, the weight decreases from *ca.* 400 to *ca.* 800 °C due to the combustion of N-G and the oxidation of Nb_4N_5. The content of N-G is calculated in detaik (see in ESI). According to the analysis and calculation, the content of N-G in Nb_4N_5/N-G is about 16.78 %.

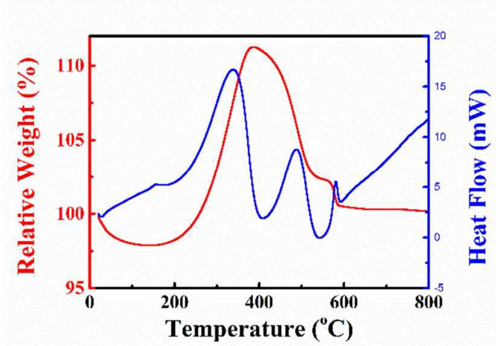

Figure 4. The TG/DSC curves of Nb_4N_5/N-G.

Three kinds of materials are examined by N_2 adsorption-desorption measurements (Figure S1). The BET surface area of bare Nb_4N_5 is 44.53 m^2 g^{-1} and the N-G is 36.86 m^2 g^{-1}. After the Nb_4N_5 is anchored on N-G, the dispersity of Nb_4N_5 loading on N-G is enhanced, so that the BET surface area increases into 49.64 m^2 g^{-1}.

Electrochemical performance

In Nb_4N_5/N-G, Li ion can intercalate first and later on under conversion reaction. During the process, a large number of Li^+ can be stored at a low potential for lithium ion battery anode material. The reaction of Nb_4N_5 and Li can be speculated as follow[23]:

$Nb_4N_5 + x Li \rightarrow Li_xNb_4N_5$ (intercalation reaction)

$Li_xNb_4N_5 + (15-x)\ Li \rightarrow 4Nb + 5Li_3N$ (conversion reaction)

The cycle voltammogram (Figure 5a) presents a stable electrochemical performance of Nb_4N_5/N-G. During the first cathodic process, two apparent cathodic peaks are observed at 1.41 V and 0.50 V (*vs.* Li/Li^+). The origin of cathodic peak at 1.41V can be attributed to the Li ion intercalation into the Nb_4N_5/N-G. The peak at 0.50 V is due to the solid electrolyte interface (SEI) formation. Furthermore, the minor slope changing at 0.15 V can be assigned to a conversion reaction from $Li_xNb_4N_5$ to Nb and Li_3N. After the 5th cycle, the peak at 1.41 V shifts to a higher potential (1.58 V) due to the difficulty of Li intercalation into residual Nb_4N_5/N-G. Similarly, the peak at 0.15 V shifts to a prominent peak at 0.17 V because of the electrode polarization. During the anodic sweep, the oxidation peak can be attributed to the oxidation reaction, from Nb^0 to $Li_xNb_4N_5$ and $Li_xNb_4N_5$ to Nb_4N_5.

To further clarify the difference of Nb_4N_5/N-G and Nb_4N_5 in electrochemical performance, electrochemical impedance spectroscopy (EIS) is carried out at frequencies from 100 kHz to 0.01 Hz to identify the correlation between the electrochemical performance and electrode kinetics. Figure 5b shows the Nyquist plots for the Nb_4N_5/N-G and Nb_4N_5 after three cycles. The Nyquist plots for Nb_4N_5/N-G and Nb_4N_5 share the similar feature of a high-frequency depressed semicircle and a medium-frequency depressed semicircle followed by a linear tail in the low-frequency region. The intercept on the Z´ axis at the high frequency end is the equivalent series resistance (R_s). The Nb_4N_5 and Nb_4N_5/N-G have a similar intercept on the Z′ axis. The size of the semicircular that includes the medium-frequency response represents charge-transfer resistance (R_{ct}). Obviously, the diameter of the semicircle for Nb_4N_5/N-G electrode is markedly lower than Nb_4N_5 in the high-frequency region. This phenomenon indicates that Nb_4N_5/N-G possesses lowest contact and charge-transfer impedances so that electron can transport rapidly during the electrochemical lithium extraction and insertion.[24] These results confirm that the disorderly wrinkle layer-to-layer N-G (likes huge charge-transfer network) can provide more active sites and greater contact area with Nb_4N_5. The inclined linear line in the low-frequency region stands for the Warburg impedance (Z_w) which relates to lithium diffusion in the solid electrode.[25] All the advantages of Nb_4N_5/N-G above result in enormous improvement of the electrochemical performance (specific capacity, rate performance, *etc.*) compared to bare Nb_4N_5.

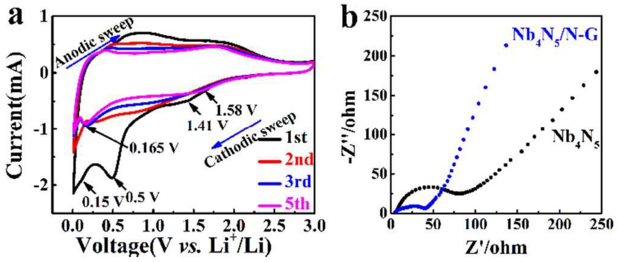

Figure 5. (a) Cyclic Voltammogram of Nb_4N_5/N-G hybrid with a scanning rate of 0.3 mV/s ranging from 0.01 to 3 V (*vs.* Li^+/Li); **(b)** Nyquist plots of Nb_4N_5/N-G and Nb_4N_5 at opening circuit voltage after 3 cycles.

Figure 6a shows galvanostatic charge profiles of Nb_4N_5/N-G electrode within the voltage of 0.01-3 V (*vs.* Li/Li^+) at a current density of 0.1 A g^{-1} (0.0819 mA cm^{-2}). The profiles are in good agreement with the CV results. Two conspicuous plateaus (1.5 and 2.2 V *vs.* Li/Li^+) are obtained during the discharge while prominent plateaus at around 2.1 V is observed in charge process. The galvanostatic charge/discharge curves of Nb_4N_5/N-G, Nb_4N_5 and N-G at a current of 0.1 A g^{-1} over a potential range of 0.01-3.0 V (*vs.*Li/Li^+) are shown in Figure 6b, Figure 6c and Figure S2, respectively. At the first cycle, the charge/discharge capacities of Nb_4N_5, N-G and Nb_4N_5/N-G are 432.4/899.2, 461.4/771.3 and 663.3/941.8 mA h g^{-1}, respectively. Apparently, the coulombic efficiency gets prodigious increasement from 48.09%, 59.8% to 70.43% which reflects synergistic effect between Nb_4N_5 and N-G. The enhanced initial coulombic efficiency may be ascribed to the catalytic sites on the surface of N-G, related to the decomposition of electrolyte occupied by Nb_4N_5.[26] This phenomenon effectively helps the formation of solid electrolyte interface (SEI) and the remission of severe volume expansion, leading a decreased irreversible capacity. Figure 5a shows that the reversible capacity of Nb_4N_5/N-G retains at 487.3 mA h g^{-1} after 200 cycles, with no capacity loss from the 20th cycle. Meanwhile, the tendency of charge-discharge curve still maintains enhanced step by step. The metal nitride reveals ordered and disordered phases with significant levels of lithium vacancies.[27] Li vacancies are the charge carriers in Li_3N, which is a well-known fast-ion conductor with the highest Li^+ conductivity.[27] The formation of additional vacancies in the nitride phases implies their potential for enhanced lithium ion diffusion. The reason why the Nb_4N_5/N-G has remarkable performance can be interpreted by following: (1) suitable kinetic reaction due to the fast diffusion of Li^+; (2) tremendous conductive network of N-G.

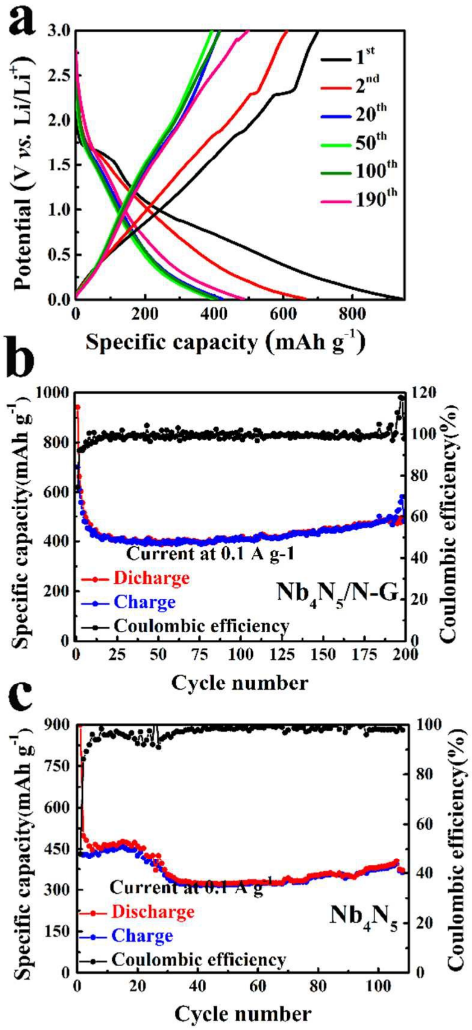

Figure 6. (a) Galvanostatic discharge-charge profiles of Nb_4N_5/N-G within the voltage window of 3.00-0.01 V at a current density of 0.1 A g^{-1} (0.0819 mA cm^{-2}); **(b)** Cycle performance and coulombic efficiency of Nb_4N_5/N-G at 0.1A g^{-1} (0.0819 mA cm^{-2}); **(c)** Cyclic performance and coulombic efficiency of Nb_4N_5 at 0.1A g^{-1} (0.0955 mA cm^{-2}).

The rate performance of Nb_4N_5/N-G with different current densities is given in Figure 7a. The incremental rates discharge capacity are 481, 430, 365, 265, 125 mA h g^{-1} at 0.2 A g^{-1} (0.1637 mA cm^{-2}), 0.5 A g^{-1} (0.4093 mA cm^{-2}), 1 A g^{-1} (0.8185 mA cm^{-2}), 2 A g^{-1} (1.6370 mA cm^{-2}), 5 A g^{-1} (4.0926 mA cm^{-2}), respectively. After high rate charge/discharge, the specific capacity of Nb_4N_5/N-G at the current density of 0.1 A g^{-1} (0.0819 mA cm^{-2}) can recover to the initial value, which confirms the structure stability. The capacity of Nb_4N_5/N-G hybrid at even 5A g^{-1} (4.0926 mA cm^{-2}) is as high as 125 mA h g^{-1} while that of Nb_4N_5 (Figure 7b) is only 70 mA h g^{-1} at the current density of 1 A g^{-1} (0.9549 mA cm^{-2}). The N-G provides enormous conductive network for Nb_4N_5, which is favorable for charge transport. The Nb_4N_5/N-G hybrid has more active sites because of the metal-rich material and N-G. After discharge, the generated Nb atoms take lower area leading fast Li^+ diffusion. The rate performance of Nb_4N_5/N-G hybrid anode further confirms the possible application for LIBs.

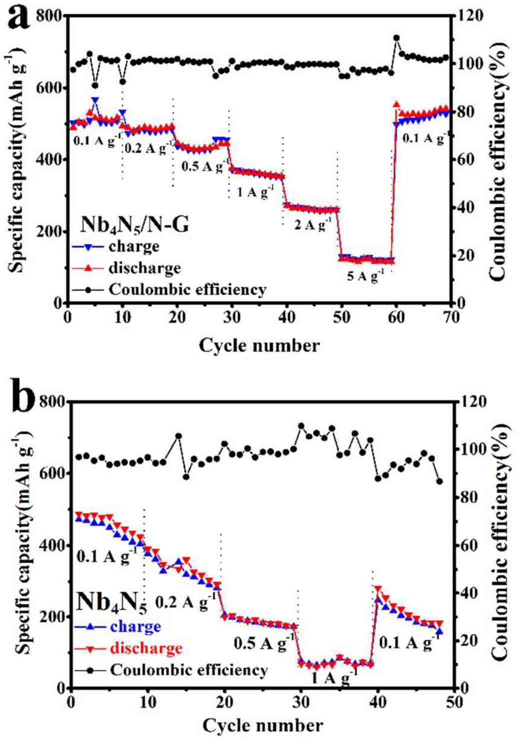

Figure 7. (a) Rate performance of Nb_4N_5/N-G at varied current density; **(b)** Rate performance of bare Nb_4N_5 at varied current density.

Conclusions

In conclusion, Nb_4N_5/N-G hybrid is successfully synthesized by a facile *in-situ* ice bathing method with subsequent annealing in NH_3. The conductive Nb_4N_5 nanocrystals are uniformly dispersed on the N-G. The Nb_4N_5 nanocrystals have mainly no band gap which make contributions to lower charge-transfer resistance and electrode polarization so that the cells have the excellent electrochemical performance.[28] The specific capacity is 487 mA h g^{-1} at 0.1 A g^{-1} (0.0819 mA cm^{-2}) which still demonstrates upgrade tendency. The hybrid also exhibits good rate capability compared to the bare Nb_4N_5 with capacity of 125 mA h g^{-1} at the current density of 5 A g^{-1}(4.0926 mA cm^{-2}). Above all, Nb_4N_5/N-G hybrid can be a novel promising anode material for LIBs with high energy density and long cycle life.

Acknowledgements

This work was financially supported from National Natural Science Foundation of China (Grant nos. 61376056, 51125006, 91122034, 51121064, 51222212), National Program of China (Grant No. 2016YFB0901600), and Science and Technology Commission of Shanghai (Grant no. 13JC1405700, 14520722000).

Notes and references

1 X. Xia, D. Chao, Y. Zhang, Z. Shen and H. Fan, *Nano Today*, 2014, **9**, 785-807.

2 G. Cui, L. Gu, L. Zhi, N. Kaskhedikar, P. A. van Aken, K. Müllen and J. Maier, *Adv Mater*, 2008, **20**, 3079-3083.

3 M. Yoshio, H. Wang, K. Fukuda, T. Umeno, T. Abe and Z. Ogumi, *Journal of Materials Chemistry*, 2004, **14**, 1754-1758.

4 H. Li, Z. Wang, L. Chen and X. Huang, *Advanced materials*, 2009, **21**, 4593.

5 G. Cui, L. Gu, A. Thomas, L. Fu, P. A. van Aken, M. Antonietti and J. Maier, *ChemPhysChem*, 2010, **11**, 3219-3223.

6 N. Suzuki, R. B. Cervera, T. Ohnishi and K. Takada, *Journal of Power Sources*, 2013, **231**, 186-189.

7 X. Lu, G. Wang, T. Zhai, M. Yu, S. Xie, Y. Ling, C. Liang, Y. Tong and Y. Li, *Nano Lett*, 2012, **12**, 5376-5381.

8 B. Das, M. Reddy, P. Malar, T. Osipowicz, G. S. Rao and B. Chowdari, *Solid State Ionics*, 2009, **180**, 1061-1068.

9 M. Wen, C. Hu, Q. Meng, Z. Zhao, T. An, Y. Su, W. Yu and W. Zheng, *Journal of Physics D: Applied Physics*, 2009, **42**, 035304.

10 H. Cui, G. Zhu, X. Liu, F. Liu, Y. Xie, C. Yang, T. Lin, H. Gu and F. Huang, *Advanced Science*, 2015, **2**(12).

11 L. Tang, Y. Wang, Y. Li, H. Feng, J. Lu and J. Li, *Advanced Functional Materials*, 2009, **19**, 2782-2789.

12 W. S. Hummers Jr and R. E. Offeman, *Journal of the American Chemical Society*, 1958, **80**, 1339-1339.

13 D. Geng, S. Yang, Y. Zhang, J. Yang, J. Liu, R. Li, T.-K. Sham, X. Sun, S. Ye and S. Knights, *Appl Surf Sci*, 2011, **257**, 9193-9198.

14 Y. T. Lee, N. S. Kim, S. Y. Bae, J. Park, S.-C. Yu, H. Ryu and H. J. Lee, *The Journal of Physical Chemistry B*, 2003, **107**, 12958-12963.

15 K. Suenaga, M. Yudasaka, C. Colliex and S. Iijima, *Chemical Physics Letters*, 2000, **316**, 365-372.

16 A. Ferrari, J. Meyer, V. Scardaci, C. Casiraghi, M. Lazzeri, F. Mauri, S. Piscanec, D. Jiang, K. Novoselov and S. Roth, *Physical review letters*, 2006, **97**, 187401.

17 A. Malesevic, R. Vitchev, K. Schouteden, A. Volodin, L. Zhang, G. Van Tendeloo, A. Vanhulsel and C. Van Haesendonck, *Nanotechnology*, 2008, **19**, 305604.

18 H. Wang, C. Zhang, Z. Liu, L. Wang, P. Han, H. Xu, K. Zhang, S. Dong, J. Yao and G. Cui, *J Mater Chem*, 2011, **21**, 5430.

19 Y. Ufuktepe, A. Farha, S. Kimura, T. Hajiri, K. Imura, M. Mamun, F. Karadag, A. Elmustafa and H. Elsayed-Ali, *Thin Solid Films*, 2013, **545**, 601-607.

20 Y. Ufuktepe, A. H. Farha, S.-i. Kimura, T. Hajiri, F. Karadağ, M. A. Al Mamun, A. A. Elmustafa, G. Myneni and H. E. Elsayed-Ali, *Materials Chemistry and Physics*, 2013, **141**, 393-400.

21 J. Alfonso, J. Buitrago, J. Torres, J. Marco and B. Santos, *Journal of materials science*, 2010, **45**, 5528-5533.

22 A. L. M. Reddy, A. Srivastava, S. R. Gowda, H. Gullapalli, M. Dubey and P. M. Ajayan, *ACS nano*, 2010, **4**, 6337-6342.

23 D. K. Nandi, U. K. Sen, D. Choudhury, S. Mitra and S. K. Sarkar, *ACS applied materials & interfaces*, 2014, **6**, 6606-6615.

24 C. He, S. Wu, N. Zhao, C. Shi, E. Liu and J. Li, *ACS nano*, 2013, **7**, 4459-4469.

25 J. Z. Wang, C. Zhong, D. Wexler, N. H. Idris, Z. X. Wang, L. Q. Chen and H. K. Liu, *Chemistry-A European Journal*, 2011, **17**, 661-667.

26 I. s. Kim, P. Kumta and G. Blomgren, *Electrochemical and Solid-State Letters*, 2000, **3**, 493-496.

27 Z. Stoeva, R. Gomez, A. G. Gordon, M. Allan, D. H. Gregory, G. B. Hix and J. J. Titman, *Journal of the American Chemical Society*, 2004, **126**, 4066-4067.

28 C. Chen, Y. Huang, H. Zhang, X. Wang, G. Li, Y. Wang, L. Jiao and H. Yuan, *Journal of Power Sources*, 2015, **278**, 693-702.